

# Supplemental Material: Evolution of the magnetic excitations in electron-doped

$\text{La}_{2-x}\text{Ce}_x\text{CuO}_4$   
(Dated: December 7, 2023)

## I. RIXS DATA NORMALIZATION

All RIXS data collected in  $\sigma$  and  $\pi$  channel was normalized to  $dd$  excitations.

## II. POLARIZATION DEPENDENCE OF THE RIXS CROSS SECTIONS

With the single ion model [1], we assume  $\text{Cu}^{2+}$  is in  $3d^9$  configuration and the unoccupied orbital is  $|d_{x^2-y^2}\rangle$ . The RIXS cross sections  $I_{\Delta S=1,0}$  of the single spin-flip process ( $\Delta S = 1$ ) and non-spin-flip process ( $\Delta S = 0$ ) for a certain spin direction are the functions of polarization and geometry of incident and scattered light. The RIXS cross section at  $L_3$  edge ( $2p_{3/2} \rightarrow 3d$ ) can be described by [1, 2],

$$I_{\Delta S=1,0}(\theta_s, \epsilon, \epsilon') \sim \left| \sum_{m=\pm\frac{3}{2}, \pm\frac{1}{2}} \langle d_{x^2-y^2}^{\downarrow(\theta_s), \uparrow(\theta_s)} | \epsilon'^* \cdot r | p_{3/2, m} \rangle \langle p_{3/2, m} | \epsilon \cdot r | d_{x^2-y^2}^{\uparrow(\theta_s)} \rangle \right|^2 \quad (\text{S1})$$

where  $\epsilon(\epsilon')$  and  $\theta_s$  are the polarization of the incident(outgoing) photon and the angle between the spin direction and c axis, respectively. The calculated cross sections  $I_{\Delta S=1,0}(\theta_s)$  for both  $\sigma$  ( $\sigma'$ ) and  $\pi$  ( $\pi'$ ) polarization of the incident(outgoing) photon are listed in table S1, where  $\alpha(\beta)$  indicates the incident(outgoing) angle. In our case, the spins are not ordered, and our detection does not discriminate the polarization of the exit light. Thus the results listed in table S2 are spin direction  $\theta_s$  and scattered photon polarization integrated.

		in	
		out	
$I_{\Delta S=1}(\theta_s)$	$\sigma'$	0	$\sin^2 \alpha \sin^2 \theta_s$
	$\pi'$	$\sin^2 \beta \sin^2 \theta_s$	0
$I_{\Delta S=0}(\theta_s)$	$\sigma'$	4	$\sin^2 \alpha \cos^2 \theta_s$
	$\pi'$	$\sin^2 \beta \cos^2 \theta_s$	$4 \sin^2 \alpha \sin^2 \beta$

TABLE S1: Cross sections for both  $\sigma(\sigma')$  and  $\pi(\pi')$  polarization of the incident(outgoing) photon calculated from single ionic model.  $\alpha(\beta)$  indicates the incident (outgoing) angle and  $\theta_s$  is the angle between spin direction and c axis.

	$\sigma$	$\pi$
$I_{\Delta S=1}$	$\frac{4}{3} \sin^2 \beta$	$\frac{4}{3} \sin^2 \alpha$
$I_{\Delta S=0}$	$8 + \frac{2}{3} \sin^2 \beta$	$\frac{2}{3} \sin^2 \alpha + 8 \sin^2 \alpha \sin^2 \beta^2$

TABLE S2: Spin direction and scattered signal polarization integrated cross section from table S1.

Thus the relative ratios of the spin-flip and non-spin-flip contributions for  $\sigma$  and  $\pi$  incident X-ray are given by

$$\frac{I_{\sigma, \Delta S=1}}{I_{\sigma, \Delta S=0}} = \frac{1}{\frac{6}{\sin^2 \beta} + 1} \quad (\text{S2})$$

$$\frac{I_{\pi, \Delta S=1}}{I_{\pi, \Delta S=0}} = \frac{1}{6 \sin^2 \beta + \frac{1}{2}} \quad (\text{S3})$$

It can be seen that the ratios only depend on the outgoing angle  $\beta$ . When the outgoing angle  $\beta$  goes to zero,  $I_{\sigma, \Delta S=1}/I_{\sigma, \Delta S=0}$  goes to zero, which means with  $\sigma$  incidence the spin-flip signal is fully suppressed. On the other hand,  $I_{\pi, \Delta S=1}/I_{\pi, \Delta S=0}$  reach its maximum in  $\pi$  incidence, which means the spin-flip signal is maximized. Thus keeping exit angle  $\beta$  small, *i.e.* grazing out geometry, and switching between incident  $\sigma$  and  $\pi$  channel offers the best separation the spin-flip and non-spin-flip processes in the RIXS spectra. We emphasize that, although the single ion model does not strictly apply to the system we studied, it serve as an useful guidance for geometry selection.

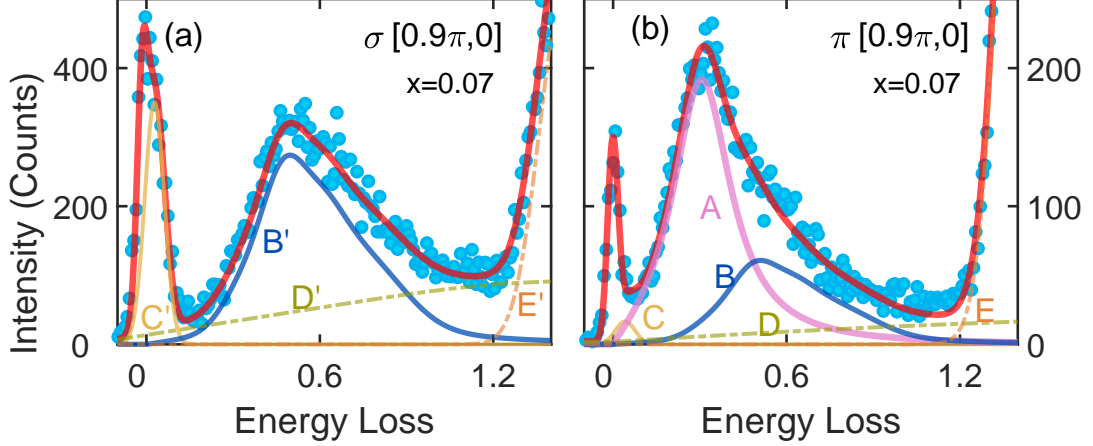


FIG. S1: Cross-fitting process for (a)  $\pi$  channel and (b)  $\sigma$  channel at  $[0.9\pi, 0]$  with  $x=0.07$ . The total fit (red) to the experiment data is obtained by the sum of several components: elastic line, phonon **C** (**C'**), paramagnon **A**, multimagnon-dominating component **B** (**B'**),  $dd$  excitation **E** (**E'**) and background **D** (**D'**).

### III. CROSS-FITTING METHOD

The raw data taken in  $\sigma$  and  $\pi$  incidence channel can be written as

$$I^{\pi, \sigma} = M^{\pi, \sigma} + I_{\text{other}}^{\pi, \sigma}$$

where  $M^{\pi, \sigma}$  indicate the paramagnon and multimagnon components which we are interested in, and  $I_{\text{other}}^{\pi, \sigma}$  include elastic peak, phonon,  $dd$  excitation and particle-hole continuum which can be fitted by simple Gaussian function and linear base. We write  $M^{\pi, \sigma}$  as a combination of the spectral weight from both spin-flip and non-spin-flip channels,

$$M^{\pi, \sigma} = R_{\text{sf}}^{\pi, \sigma} \cdot S_{\text{sf}} + R_{\text{nf}}^{\pi, \sigma} \cdot S_{\text{nf}} \quad (\text{S4})$$

We first extract the line shape of  $M^{\sigma}$  from data collected with  $\sigma$  incidence in which case the multimagnon component dominates, and this is demonstrated in Fig. S1(a). The spectrum is decomposed into elastic peak, multimagnon-dominating component **B'** corresponding to  $M^{\sigma}$ , linear base **D'** and  $dd$  excitation **E'**. The elastic peak and  $dd$  peak are fitted by Gaussian function. The multimagnon-dominating component **B'** is fitted with a free line-shape function, which includes arbitrary multiple peaks necessary to account the overall spectral curve. With **B'** obtained, it is used as the input to fit the spectra collected with  $\pi$  incidence with a fitting parameter  $b$ . The overall spectra from  $\pi$  incidence are

$$I^{\pi} = a \cdot S_{\text{sf}} + b \cdot M^{\sigma} + \mathbf{C} + \mathbf{D} + \mathbf{E} \quad (\text{S5})$$

where  $a = R_{\text{sf}}^{\pi} - R_{\text{sf}}^{\sigma} R_{\text{nf}}^{\sigma} / R_{\text{nf}}^{\pi}$ ,  $b = R_{\text{nf}}^{\pi} / R_{\text{nf}}^{\sigma}$  and the spin-flip component  $S_{\text{sf}}$  in our fitting is described by a damped harmonic oscillator function (see Sec. IV). Such fitting approach is demonstrated in Fig. S1(b). By this cross-fitting method, we separate the pure paramagnon **A** from multimagnon component. The fitting quality of such cross-fitting method for all data presented are shown in Fig. S2.

For comparison, we also did a simple fitting following the previous work [3]. And the results are shown in Fig. S3. Here all components are fitted by Gaussian functions.

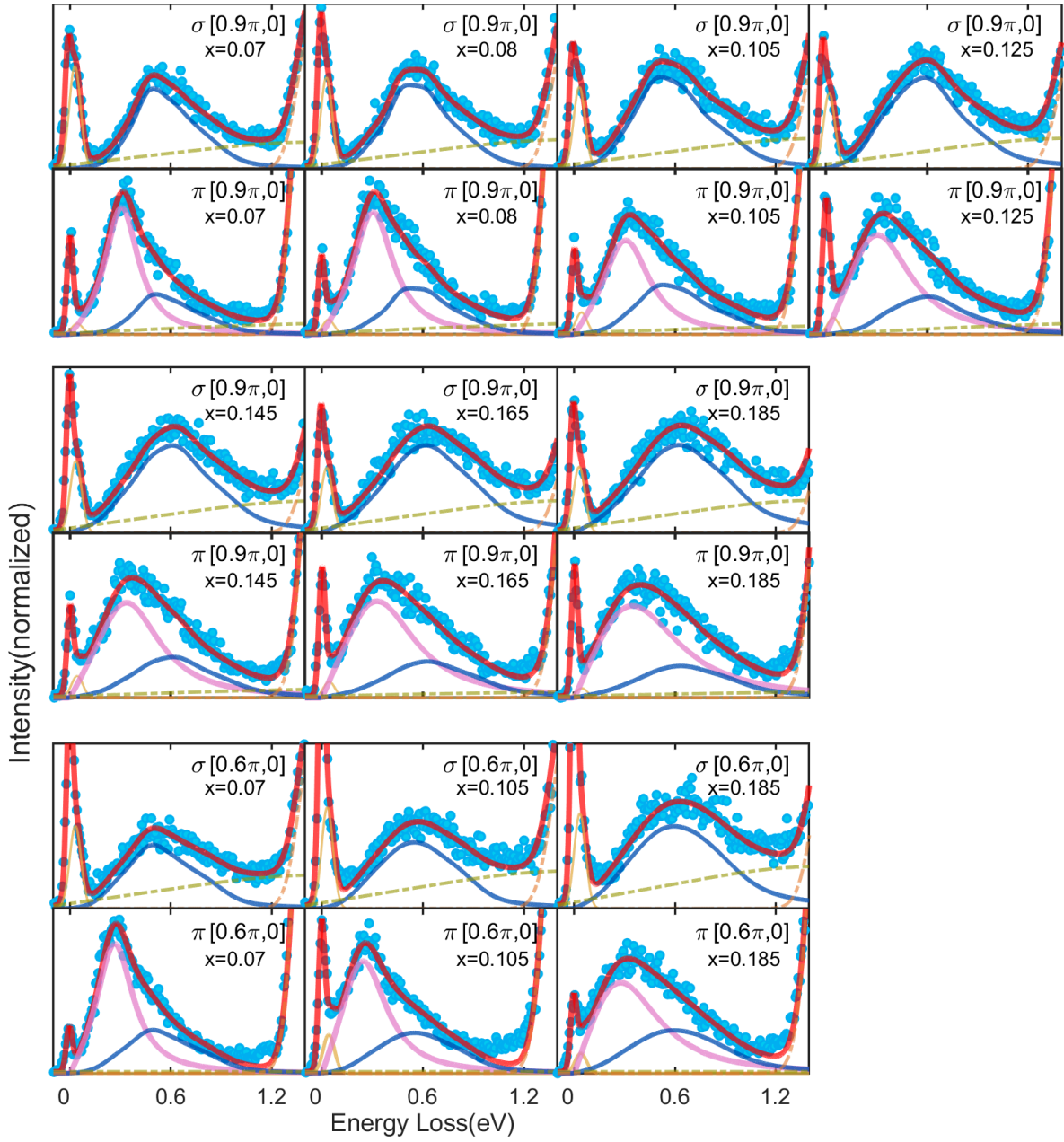


FIG. S2: Cross-fitting method shown in Fig. S1 for doping varying from  $x = 0.07$  to  $x = 0.185$  at  $[0.9\pi, 0]$  and  $[0.6\pi, 0]$ .

#### IV. DAMPED HARMONIC OSCILLATOR

The spin-flip contribution is fitted with a damped harmonic oscillator function,

$$\begin{aligned}
 f(\omega) &= \frac{A_0}{1 - e^{-\beta\hbar\omega}} \frac{4\omega\Gamma_q\omega_0}{(\omega^2 - \omega_0^2)^2 + (2\omega\Gamma_q)^2} \\
 &= \frac{A_0}{1 - e^{-\beta\hbar\omega}} \frac{4\omega\Gamma_q\sqrt{\omega_q^2 + \Gamma_q^2}}{(\omega^2 - \omega_q^2 - \Gamma_q^2)^2 + (2\omega\Gamma_q)^2} \\
 &= \frac{A_q}{1 - e^{-\beta\hbar\omega}} \left( \frac{\Gamma_q}{\Gamma_q^2 + (\omega - \omega_q)^2} - \frac{\Gamma_q}{\Gamma_q^2 + (\omega + \omega_q)^2} \right)
 \end{aligned} \tag{S6}$$

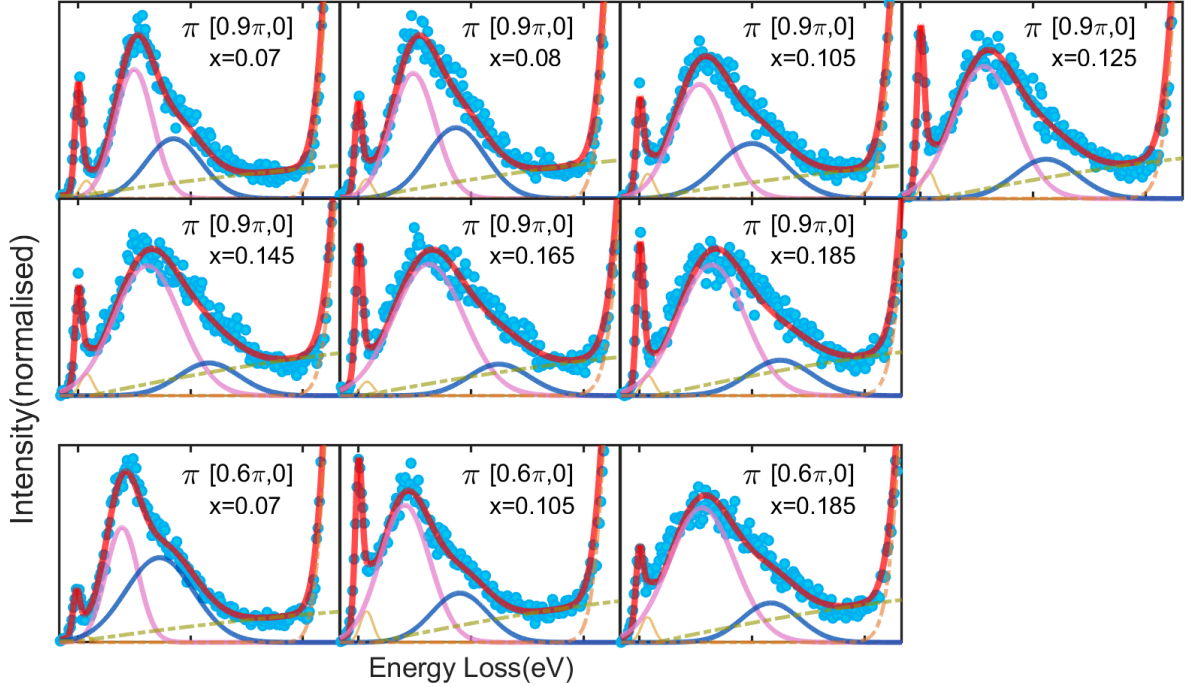


FIG. S3: Simple Gaussian fitting to  $\pi$  channel only for doping varying from  $x=0.07$  to  $x=0.185$  at  $[0.9\pi, 0]$  and  $[0.6\pi, 0]$  as a comparison with Fig. S2. Similar to the former, pink line is referred as paramagnon component.

where  $\omega_q = \sqrt{\omega_0^2 - \Gamma_q^2}$  is the propagating frequency (the real part of the damped harmonic oscillator pole  $\omega_p = \pm\sqrt{\omega_0^2 - \Gamma_q^2} + i\Gamma_q$ ), and  $A_q = A_0 \cdot \omega_0/\omega_q$ . In our fitting,  $\omega_0$  is always larger than  $\Gamma_q$ , suggesting the measured spin-flip excitations in our doping range are propagating excitations.

The maximum of the peak is given by

$$\omega_{\max} = \sqrt{\frac{1}{3} \left( \omega_q^2 - \Gamma_q^2 + 2\sqrt{\omega_q^4 + \omega_q^2\Gamma_q^2 + \Gamma_q^4} \right)}$$

which is larger than  $\omega_q$  [4].

The obtained doping dependence of  $A_q$  is shown in fig. S4(a) and S4(c). At both  $\mathbf{Q}_{\parallel}$  points,  $A_q$  increases strongly as function of doping. Such increasing is required by the experimental observed spectral weight evolution. Once the fitted damped harmonic contribution is *normalized* by  $A_q$  to remove its scaling effect (fig. S4(b) and fig. S4(d)), the resulted spectra are strongly compressed at higher doping, inconsistent with the experiment observation.

## V. CONSIDERATION ON THE SELF-ABSORPTION EFFECT

The grazing out geometry employed is important for our cross-fitting approach, but it also brings enhanced self-absorption effect for the scattered signal during its out-going path through the sample. The impact from the self-absorption is discussed in this section. Before the details, we make the statement that the self-absorption is not critical to our analysis and conclusions.

If we assume the absorption coefficient  $\mu(\omega)$  for the photons in the energy range of our interest is energy-independent, the self-absorption will act as just an overall normalization factor to our data with the fixed grazing-exit angle geometry. So the question becomes: how significant is the variation of the  $\mu(\omega)$  as a function of energy in the range of our interest. Ideally it would be preferable to directly measure the  $\mu(\omega)$  on our sample. But LCCO has to be stabilized on a substrate from PLD growth, so it is impossible to perform a “true” absorption measurement which requires transmission geometry. Total electron yield measurements are surface sensitive and probe a different volume to that studied in RIXS. Total fluorescence yield measurements suffer from (i) self-absorption effect related distortions and (ii) changes in the ratio of fluorescent and Auger processes through the absorption edges.

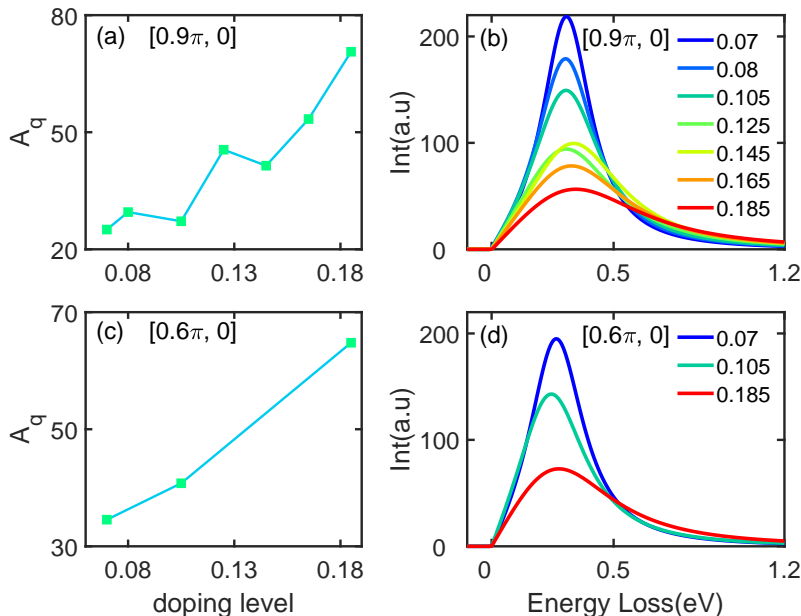


FIG. S4: The evolution of fitting parameter  $A_q$  upon doping is shown in (a) for  $\mathbf{Q}_{\parallel} = [0.9\pi, 0]$  and (c) for  $\mathbf{Q}_{\parallel} = [0.6\pi, 0]$ , respectively. The line-shape of single magnon component normalized by  $A_q$  are shown in (b) for  $\mathbf{Q}_{\parallel} = [0.9\pi, 0]$  and (d) for  $\mathbf{Q}_{\parallel} = [0.6\pi, 0]$ , respectively.

To properly evaluate the self-absorption effect, we checked two independent procedures to estimate  $\mu(\omega)$  from x-ray fluorescence, which give consistent results. Data fitting with estimated absorption correction is also given.

The calculated X-ray attenuation length for LCCO from the center for X-ray Optics(CXRO) [6] is shown in the upper panel of fig. S5. Although there is a clear jump at the Cu- $L$  edge, the major absorption channels around 930eV are from O and La, with certain contribution from Ce. We are aware that there are published attempts to make self-absorption correction to the cuprate RIXS signal by assuming the measured fluorescence yield signal is proportional to the  $\mu(\omega)$  [7–9]. On the other hand, it is known that, if there are multiple fluorescence emission channels, the assumption that  $\mu(\omega)$  is proportional to the measured total fluorescence yield signal is questionable [5].

The CXRO calculation is based on the tabled values by B.L. Henke, E.M. Gullikson, and J.C. Davis [10], which catches the core hole to continuum absorption channels well but cannot describe the near  $L$ -edge resonant feature  $\mu(\omega \sim \omega_{\text{res}})$ . To get the  $\mu(\omega)$  of the  $L$ -edge, one needs more specialized measurements.

An elegant work along this line was presented by A. J. Achkar *et al* [5]. They used the so called inverse-partial-fluorescence-yield (IPFY) technique to extract the total x-ray absorption coefficient  $\mu(\omega)$  for NiO across the Ni- $L$  edges. This measurement is technically more demanding, but the multiple fluorescence emission channel mixing problem is avoided. As a result, they obtained the  $\mu(\omega)$  as shown in the lower panel of fig. S5. The green line is from CXRO calculation, and the multiple-overlapping lines are the extracted total  $\mu(\omega)$  from data at different measurement geometries. At the pre-edge around 845eV,  $\mu^{\text{NiO}}(\omega_{\text{pre}})$  is  $2.2\mu\text{m}^{-1}$ , the continuum absorption channels from Ni contributes a step of  $\Delta\mu^{\text{NiO}} = \mu^{\text{NiO}}(\omega_{\text{post}}) - \mu^{\text{NiO}}(\omega_{\text{pre}}) = 6.1\mu\text{m}^{-1}$ . At the Ni  $L_3$ -edge resonant peak, the total  $\mu^{\text{NiO}}(\omega_{\text{res}} \sim 854\text{eV})$  reaches  $31.0\mu\text{m}^{-1}$ .

We use the above as a guidance to estimate the  $\mu(\omega)$  for our sample. In NiO, Ni is in an oxygen octahedral coordinate environment. Thus the Ni-orbital configuration is similar to Cu in LCCO. For LCCO, CXRO calculations indicate  $\mu^{\text{LCCO}}(\omega_{\text{pre}}) = 5.4\mu\text{m}^{-1}$  and a continuum step of  $\Delta\mu^{\text{LCCO}} = \mu^{\text{LCCO}}(\omega_{\text{post}}) - \mu^{\text{LCCO}}(\omega_{\text{pre}}) = 1.2\mu\text{m}^{-1}$ . Considering the atom-per-unit-volume ratio of Cu-in-LCCO: Ni-in-NiO is about 1: 5.1, this is consistent with the  $1.2:6.1 = 1:5.08$  ratio of the continuum absorption steps in the two materials. With this discussion base set, we assume the  $d$  orbital partial absorption coefficient vs. continuum absorption steps ratios are the same for Ni- $L$  edge in NiO and Cu- $L$  edge in LCCO, and consider there are two unoccupied  $d$  states in NiO and one unoccupied  $d$  states in LCCO. As a result, we can have the following relation:

$$2 \left( \frac{\mu^{\text{LCCO}}(\omega_{\text{res}}) - \mu^{\text{LCCO}}(\omega_{\text{pre}})}{\mu^{\text{LCCO}}(\omega_{\text{post}}) - \mu^{\text{LCCO}}(\omega_{\text{pre}})} \right) = \frac{\mu^{\text{NiO}}(\omega_{\text{res}}) - \mu^{\text{NiO}}(\omega_{\text{pre}})}{\mu^{\text{NiO}}(\omega_{\text{post}}) - \mu^{\text{NiO}}(\omega_{\text{pre}})} \quad (\text{S7})$$

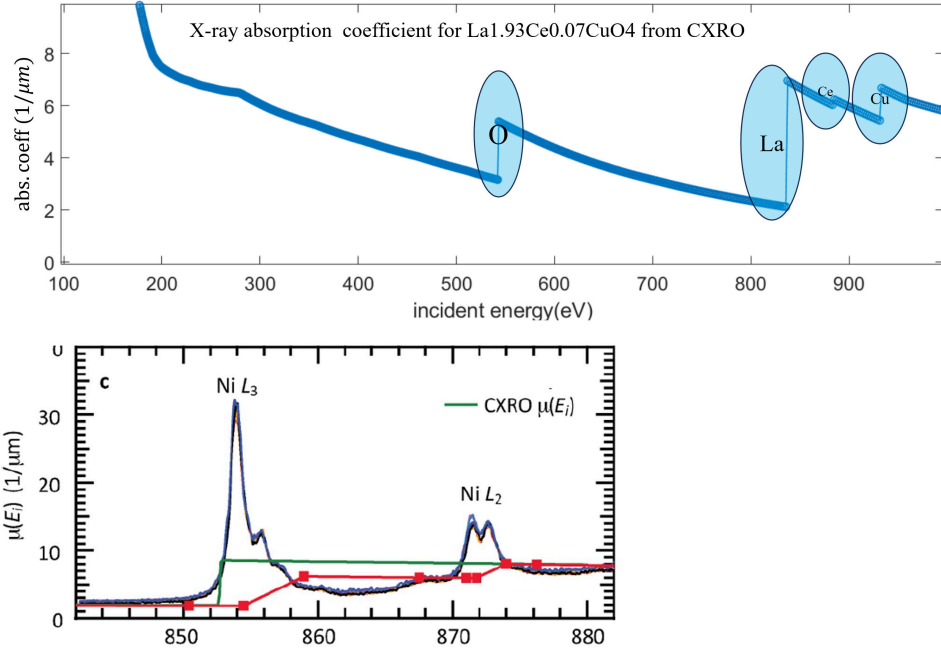


FIG. S5: Upper panel: simulated X-ray absorption coefficient for LCCO from CXRO. lower panel: total absorption coefficient  $\mu(\omega)$  for NiO using inverse partial fluorescence yield (IPFY) method [5]. The green line is from CXRO calculation and the multiple-overlapping lines are the extracted  $\mu(\omega)$  at different measurement geometries.

Thus for LCCO ( $x = 0.07$ ) at  $\text{Cu-}L_3$  resonant peak, the total absorption coefficient comes out as

$$\mu^{\text{LCCO}}(\omega_{\text{res}}) = 8.2 \mu\text{m}^{-1}$$

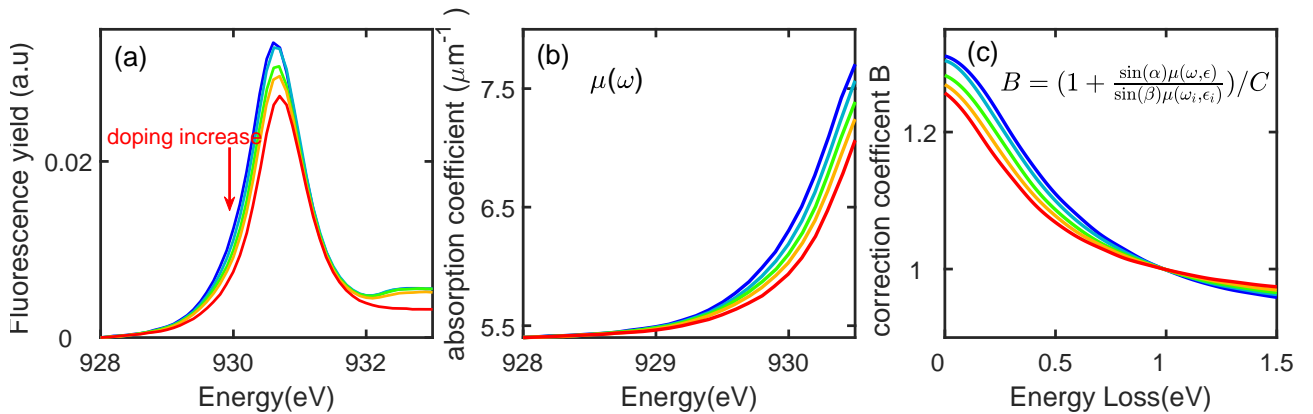


FIG. S6: (a) Fluorescence yield signal of LCCO for different doping levels. (b) The estimated absorption coefficient extracted from Fluorescence yield by eq. S8. (c) The absorption correction  $B = (\frac{\sin \alpha}{\sin \beta} \cdot \frac{\mu(\omega, \epsilon)}{\mu(\omega_i, \epsilon_i)} + 1)/C$ , where  $C$  ratio is applied to make  $B$  equal 1 at energy loss of 1eV, setting an anchor point for better view and comparison with data before correction.

With the above discussion, we now examine our fluorescence yield data on LCCO at grazing-in geometry with incident angle of 16 degrees and out-going angle of 114 degrees (S6(a)). This geometry much reduces the complexity from multiple fluorescence emission channel mixing as the incident beam path absorption is the leading effect. We assume:

- 1) the above derived values are good numbers for the  $\mu(\omega)$  of pre-edge and on the  $\text{Cu-}L_3$  edge fluorescence peak;
- 2) in the narrow energy range of the fluorescence peak rising edge, the variation of  $\mu(\omega)$  is proportional to the relative increasing of the total fluorescence yield strength. Thus we have the following equation:

$$\frac{\mu^{\text{LCCO}}(\omega) - \mu^{\text{LCCO}}(\omega_{\text{pre}})}{\mu^{\text{LCCO}}(\omega_{\text{res}}) - \mu^{\text{LCCO}}(\omega_{\text{pre}})} = \frac{I^{\text{LCCO}}(\omega) - I^{\text{LCCO}}(\omega_{\text{pre}})}{I^{\text{LCCO}}(\omega_{\text{res}}) - I^{\text{LCCO}}(\omega_{\text{pre}})} \quad (\text{S8})$$

where  $I^{\text{LCCO}}(\omega)$  is the intensity of fluorescence yield. With eq. S8, the  $\mu^{\text{LCCO}}(\omega)$  of different doping is extracted, which is shown in fig. S6(b). From these  $\mu(\omega)$  values, we can obtain the corrected RIXS spectra  $I_{\text{cor}}^{\text{RIXS}}$  by multiplying the experimental data with the correction coefficient

$$I_{\text{cor}}^{\text{RIXS}} = I^{\text{RIXS}} \cdot B$$

$$B = \left( \frac{\sin \alpha}{\sin \beta} \cdot \frac{\mu(\omega, \epsilon)}{\mu(\omega_i, \epsilon_i)} + 1 \right) / C \quad (\text{S9})$$

where  $\mu(\omega_i, \epsilon_i)$  is the absorption coefficient for the incident X-ray. An additional  $C$  ratio is applied to make  $B$  equal 1 at energy loss of 1eV, setting an anchor point for better view and comparison with data before correction. The correction coefficient  $B$  for different doping level are shown in fig. S6(c).

We emphasize that this  $\mu(\omega)$  reduction is an estimation, rather than a quantitatively precise procedure. But it can give an adequate evaluation of the impact of the self-absorption correction to our analysis. We note that the self-absorption correction package FLUO developed by Daniel Haskel [11] gives a similar correction coefficient as we present here, which serves as a good cross-checking.

The whole data set is re-fit with the above corrections. The comparison of the corrected data and fitting results to those without correction are shown in fig. S7. We see that there is an overall down shift of the obtained  $\omega_q$  and  $\omega_{\text{max}}$  of a few *meVs*, while the doping dependent behavior has no qualitative difference from our original fitting results. Although we believe the above correction deduction is quite reasonable for self-absorption effect evaluation, the numbers are not from a designed and controlled measurements. Thus we prefer to present the original fitting results in the main text.

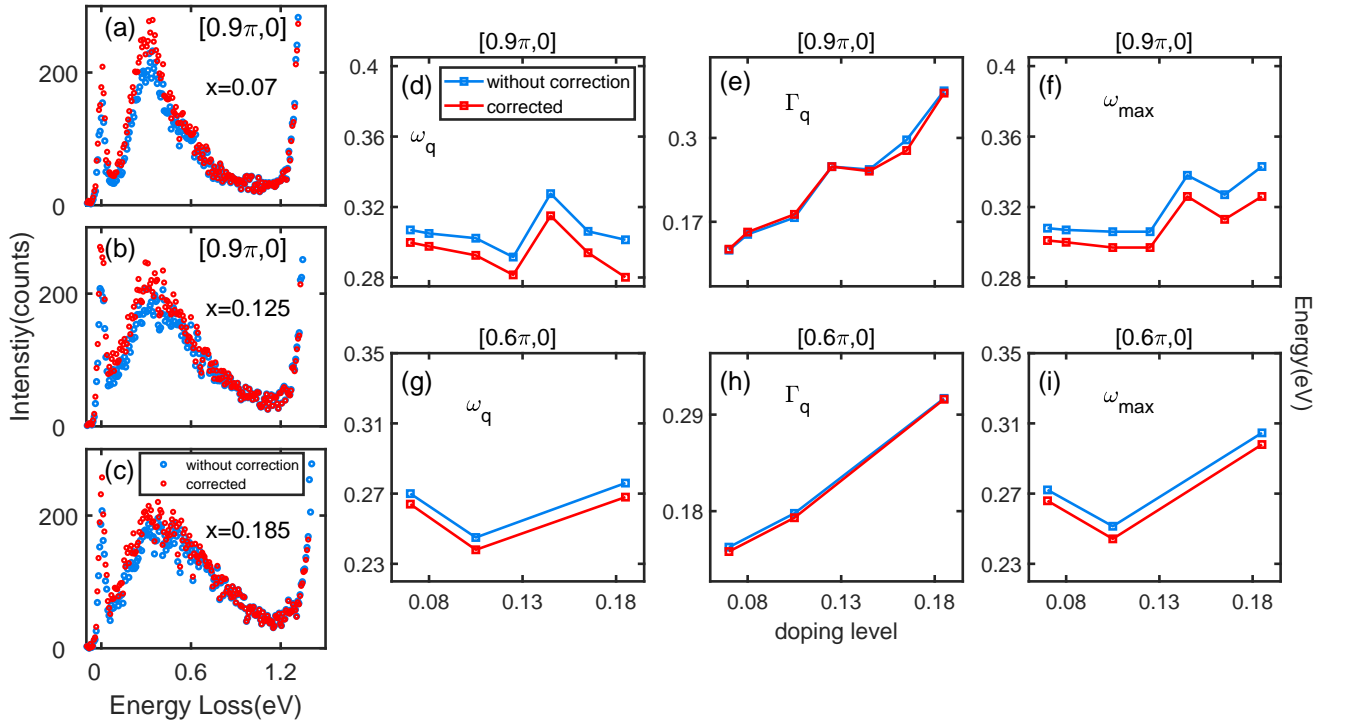


FIG. S7: The comparison of the corrected data and fitting results to those without correction . The spectra are shown in (a)-(c) and the evolution of fitting parameters upon doping are shown in (d)-(i).

- 
- [1] L. J. P. Ament, G. Ghiringhelli, M. M. Sala, L. Braicovich, and J. van den Brink, Theoretical demonstration of how the dispersion of magnetic excitations in cuprate compounds can be determined using resonant inelastic x-ray scattering, *Phys. Rev. Lett.* **103**, 117003 (2009).
- [2] M. Moretti Sala, V. Bisogni, C. Aruta, G. Balestrino, H. Berger, N. B. Brookes, G. M. d. Luca, D. Di Castro, M. Grioni, M. Guarise, P. G. Medaglia, F. Miletto Granozio, M. Minola, P. Perna, M. Radovic, M. Salluzzo, T. Schmitt, K. J. Zhou, L. Braicovich, and G. Ghiringhelli, Energy and symmetry of dd excitations in undoped layered cuprates measured by Cu  $L_3$  resonant inelastic x-ray scattering, *New Journal of Physics* **13**, 043026 (2011).
- [3] W. S. Lee, J. J. Lee, E. A. Nowadnick, S. Gerber, W. Tabis, S. W. Huang, V. N. Strocov, E. M. Motoyama, G. Yu, B. Moritz, H. Y. Huang, R. P. Wang, Y. B. Huang, W. B. Wu, C. T. Chen, D. J. Huang, M. Greven, T. Schmitt, Z. X. Shen, and T. P. Devereaux, Asymmetry of collective excitations in electron- and hole-doped cuprate superconductors, *Nature Physics* **10**, 883 (2014).
- [4] Y. Y. Peng, E. W. Huang, R. Fumagalli, M. Minola, Y. Wang, X. Sun, Y. Ding, K. Kummer, X. J. Zhou, N. B. Brookes, B. Moritz, L. Braicovich, T. P. Devereaux, and G. Ghiringhelli, Dispersion, damping, and intensity of spin excitations in the monolayer  $(\text{Bi,Pb})_2(\text{Sr,Lu})_2\text{CuO}_{6+\delta}$  cuprate superconductor family, *Phys. Rev. B* **98**, 144507 (2018).
- [5] A. J. Achkar, T. Z. Regier, E. J. Monkman, K. M. Shen, and D. G. Hawthorn, Determination of total x-ray absorption coefficient using non-resonant x-ray emission, *Scientific Reports* **1**, 182 (2011).
- [6] [the Center for X-ray Optics](#).
- [7] M. Minola, G. Dellea, H. Gretarsson, Y. Y. Peng, Y. Lu, J. Porras, T. Loew, F. Yakhov, N. B. Brookes, Y. B. Huang, J. Pellicciari, T. Schmitt, G. Ghiringhelli, B. Keimer, L. Braicovich, and M. Le Tacon, Collective nature of spin excitations in superconducting cuprates probed by resonant inelastic x-ray scattering, *Phys. Rev. Lett.* **114**, 217003 (2015).
- [8] R. Fumagalli, L. Braicovich, M. Minola, Y. Y. Peng, K. Kummer, D. Betto, M. Rossi, E. Lefrançois, C. Morawe, M. Salluzzo, H. Suzuki, F. Yakhov, M. Le Tacon, B. Keimer, N. B. Brookes, M. M. Sala, and G. Ghiringhelli, Polarization-resolved Cu  $L_3$ -edge resonant inelastic x-ray scattering of orbital and spin excitations in  $\text{NdBa}_2\text{Cu}_3\text{O}_{7-\delta}$ , *Phys. Rev. B* **99**, 134517 (2019).
- [9] H. C. Robarts, M. Barthélemy, K. Kummer, M. García-Fernández, J. Li, A. Nag, A. C. Walters, K. J. Zhou, and S. M. Hayden, Anisotropic damping and wave vector dependent susceptibility of the spin fluctuations in  $\text{La}_{2-x}\text{Sr}_x\text{CuO}_4$  studied by resonant inelastic x-ray scattering, *Phys. Rev. B* **100**, 214510 (2019).
- [10] B. L. Henke, E. M. Gullikson, and J. C. Davis, X-ray interactions: Photoabsorption, scattering, transmission, and reflection at  $e = 50\text{-}30,000$  eV,  $z = 1\text{-}92$ , *Atomic Data and Nuclear Data Tables* **54**, 181 (1993).
- [11] D. Haskel, [FLUO:Correcting XANES For self-absorption in fluorescence measurements](#).